Karlsruher Institut für Technologie
Institut für Baustatik

KIT
Karlsruher Institut für Technologie

Damage Sensitivity of Axially Loaded Stringer-Stiffened Curved CFRP Panels

S. Lauterbach, A.C. Orifici, W. Wagner, C. Balzani, H. Abramovich, R. Thomson

Mitteilung 2(2010)

BAUSTATIK

Karlsruher Institut für Technologie
Institut für Baustatik

Damage Sensitivity of Axially Loaded Stringer-Stiffened Curved CFRP Panels

S. Lauterbach, A.C. Orifici, W. Wagner, C. Balzani, H. Abramovich, R. Thomson

Mitteilung 2(2010)

BAUSTATIK

Prof. Dr.–Ing. W. Wagner
Institut für Baustatik
© Karlsruher Institut für Technologie
Kaiserstr. 12
76131 Karlsruhe

Telefon: (0721) 608–2280
Telefax: (0721) 608–6015
E–mail: bs@.uni-karlsruhe.de
Internet: http://www.bs.uni-karlsruhe.de

Damage Sensitivity of Axially Loaded Stringer-Stiffened Curved CFRP Panels

S.Lauterbach[1], A.C.Orifici[2,3], W.Wagner[1], C.Balzani[1], H.Abramovich[4], R.Thomson[3]

[1]Karlsruhe Institute of Technology(KIT), Institute for Structural Analysis, Kaiser-str.12, 76131 Karlsruhe, Germany

[2]School of Aerospace, Mechanical and Manufacturing Engineering, Royal Melbourne Institute of Technology, GPO Box 2476V, Melbourne, Victoria 3001, Australia

[3]Cooperative Research Centre for Advanced Composite Structures Ltd, 506 Lorimer Street, Fishermans Bend, Melbourne, Victoria, 3207, Australia

[4]Faculty of Aerospace Engineering, Technion - Israel Institute of Technology, Technion City, Haifa 32000, Israel

Abstract A fuselage representative carbon fibre-reinforced multi-stiffener panel is analysed under compressive loading. An intact and pre-damaged configuration is loaded into the postbuckling region and further on until collapse occurs. An analysis tool is applied that includes an approach for predicting interlaminar damage initiation and degradation models for capturing interlaminar damage growth as well as in-plane damage mechanisms. Analysis of the intact panel configuration predicts collapse due to fibre fracture in the stiffeners close to the panel clamps, which agrees well with the results from experimental testing. The pre-damaged configuration was proposed containing Teflon-coated layers to generate the initial debonds in the skin-stiffener interface. The outcome of the simulation of this configuration shows that crack growth is not predicted to occur, which agrees with the observations of the experiment. A parametric study is conducted to investigate the effect of the skin-stiffener debond parameters such as length, width and location on crack growth and the collapse behaviour of the panel. It is found that the sensitivity of the panel design to the damage parameters is highly dependent on the postbuckling mode shape or displacement pattern, and particularly the extent to which this influences the conditions at the crack front. More broadly, the analysis tool is shown to be capable of capturing the critical damage mechanisms leading to structural collapse of stiffened composite structures in the postbuckling region.

Keywords Structural composites, Delamination, Damage tolerance, Buckling, Finite element analysis (FEA)

1 Introduction

In recent years carbon fibre-reinforced polymers (CFRP) emerged in aerospace engineering. Due to their high specific strength and stiffness these composites offer considerable advantages compared to metals. A further approach namely postbuckling is to design structures that can withstand high loads even after they have buckled. The concept of postbuckling design offers possibilities to improve the structural efficiency, particularly in combination with composite materials. By allowing buckling in a structure, the ultimate load can be increased. Metals, unlike composites, offer plasticity effects to evade high stress concentrations during postbuckling. Under compressive load, composite structures show a wide range of damage mechanisms where a set of damage modes combined together might lead to the eventual structural collapse. The COCOMAT (Improved MATerial Exploitation at Safe Design of COmposite Airframe Structures by Accurate Simulation of Collapse) project [10] deals with this issue to capture the different damage mechanisms in the postbuckling region and to improve the prediction of failure. In this work different panel configurations are investigated as they were proposed within COCOMAT. For an efficient design of composite structures, damage modes have to be taken into account. There are degradation models for ply failure of a laminate, e.g. fibre fracture and matrix cracking, and interlaminar failure, namely delamination. Due to high stress gradients at the crack tip the fracture mechanics approach, e.g. [14], is often applied in finite element (FE) simulations [25] to realise crack growth between two adjacent plies within laminates. There are different possibilities to model the crack growth approach in FE. The *cohesive crack model* [2, 3, 5, 6, 11, 32] and the *virtual crack closure technique* (VCCT) [18, 29] are two of them and present the most commonly used approaches. Both of them act in the interface between two adjacent plies or sublaminates, where the connectivity of the interface is controlled in order to model crack growth. Examples of this include cohesive models implemented using springs [5] or 8-node elements [19, 24] and the VCCT applied with multipoint contraints (MPCs) [27]. The VCCT is a highly successful technique that has been used by many authors in research and industry to predict interlaminar crack growth in composite structures. In terms of many previous successful applications of this method, in the present work the VCCT is used to simulate the progress of delamination of initial debonded areas.

2 Panel Design

A fuselage representative CFRP panel is investigated. The panel is made from carbon/epoxy IM7/8552 unidirectional prepreg tape and consists of a thin curved skin co-cured to five blade stiffeners (T-shaped). All material properties are taken from characterisation tests performed by the COCO-MAT partners. The strength properties were previously presented by [9]. All parameters are summarised in Table 1. Both ends are encased in a resin potting to ensure a uniform load application. The longitudinal edges of the panel are supported to simulate the behaviour of an entire cylinder. In detail, the circumferential displacements and the rotations around the longitudinal axis are constrained. During the experimental tests, the bottom potting is clamped and the opposite side is loaded displacement controlled up to structural collapse. The symmetrical lay-up for the skin is $[0, -45, 45, 90]_s$ and the stiffener lay-up is $[(-45, 45, 0_2)_3]_s$.

The panel was manufactured in an intact and a pre-damaged configuration.

Table 1: Material properties for IM7/8552 plies (moduli and strengths in [MPa])

Elastic Properties		Strength Parameters	
E_{11}	147 000	X_t	2 670
E_{22}	11 800	X_c	1 680
ν_{12}	0.3	$Y_t = Z_t$	61
G_{12}	6 000	$Y_c = Z_c$	308
G_{23}	4 000	S_{12}	105
G_{13}	6 000	$S_{13} = S_{23}$	124

The experimental set-up and the nominal dimensions for both panel configurations are given in Fig. 1. The pre-damaged configuration, denoted by version 1, includes pre-existing skin-stiffener debonds which are generated by embedding Teflon-coated layers in the skin-stiffener interface. Three different locations of initial debonds were previously specified, see in Fig. 2, with different width across the stiffener flange. A half-width debond centred underneath the blade (20 mm), a full width debond (40 mm) and a half-width debond under one side of the flange (15 mm). Fig. 2 depicts the investigated panel including the different locations where the initial debonded regions are

Parameter	Value [mm]
Length, L	720
Free length, L_f	660
Panel radius, R	938
Stiffener pitch, b	136
Arc length, W	680
Ply thickness	0.125
Stiffener height, h	20
Stiffener width, w	40
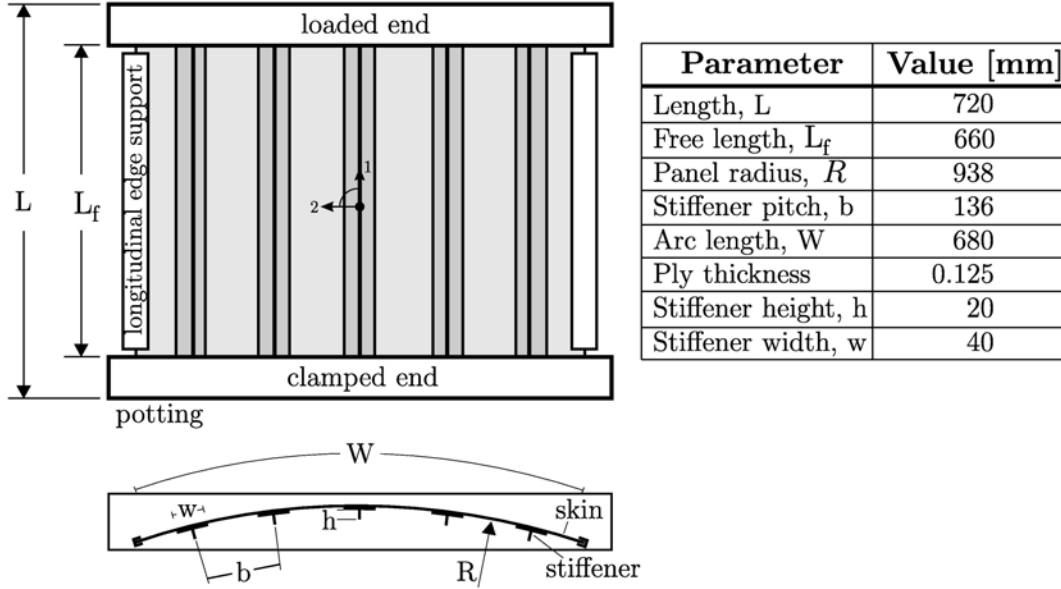
Figure 1: Experimental set-up and dimensions in [mm] for both intact and pre-damaged configuration

embedded in the skin-stiffener interface as well as the different type of pre-existing debonds. Type 1 was applied on the left-hand side, type 2 at the middle stiffener and type 3 at the outermost stiffener on the right-hand side of the panel. This staggered version offers a common initial pre-damaged length of 25 mm for all applied debonds. The centre of both upper debonds are located 210 mm away from the upper edge including the resin potting. The centre of the debond at the middle stiffener is aligned with the centreline of the panel (360 mm away from both edges).

3   Analysis Approach

An FE tool is applied to predict the collapse of stiffened composite structures in compression by capturing the effects of the critical damage mechanisms. The approach, which has been presented previously [26, 27], contains several aspects such as predicting the onset of interlaminar damage in intact structures as well as the propagation of pre-existing interlaminar damage regions and the in-plane degradation model. Even though a number of factors
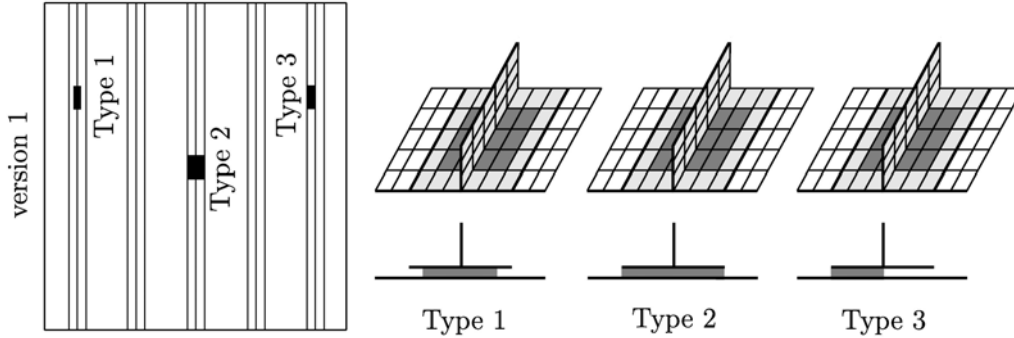
Figure 2: Pre-damaged panel configuration: Applied locations of the three different types of pre-existing debonds

such as matrix-curing shrinkage, manufacturing defects and residual thermal stresses [7] develop during the manufacturing process, they are omitted in the present work.

All models are run on a 2.4 GHz Dual Core AMD Opteron processor using the nonlinear solver in MSC.Marc 2005 [1], with a full Newton-Raphson procedure applied, a tolerance of 0.001 on load residuals, and numerical damping applied as well. All analyses are driven displacement controlled and use an adaptive load step approach to reduce the step size for recomputing when convergence failed. Detailed information on MSC.Marc algorithm is given in [1].

The approach for predicting the initiation of interlaminar damage in the skin-stiffener interface is based on a structural zooming analysis. In this technique, a global shell model is used to determine the deformation field of the entire structure, which is then applied as boundary conditions to a local 3-dimensional brick element model of the skin stiffener interface. Though various strength-based criteria are found in literature, due to the fact that each criterion differs mainly in addition of the longitudinal tensile component which is almost negligible for 2-D specimens, there is no recognisable difference between these criteria [12]. The "degenerated Tsai" criterion [30] was chosen based on simplicity and capturing all necessary effects. From this it follows, delamination prediction is only investigated using the "degenerated Tsai" criterion. This criterion is applied to monitor locations where high through-thickness stresses occur which lead to the onset of delamination most likely. Failure was deemed to occur when the average of all integration

point values in an element satisfies this criterion.

Generally, MPCs are applied to connect nodes of different surfaces including their degrees of freedom in a finite element mesh. These elements are often used to simulate a boundary condition effect when regular boundary conditions will not provide the correct behaviour. However, fracture mechanics can be applied with MPCs so that disconnection of the MPCs can take place under certain circumstances. For the propagation of interlaminar damage an FE model is generated with nominally coincident shell layers of skin and stiffener which are connected by MPCs. Gap elements are used in any region where crack growth could occur to prevent any crossover or interpenetration of the two shell layers. At the end of every nonlinear increment the VCCT is used to determine the strain energy release rates of all MPCs at the crack front. In this work the VCCT is the focus, though the related techniques are briefly introduced. The VCCT is based on the crack closure method (CCM) or two-step crack closure technique. Both approaches are based on Irwin's crack closure integral which assumes that the energy released when the crack is extended by a certain length is identical to the energy required to close the crack again [17]. The CCM and the two-step crack closure technique need two computational runs at each increment. In the first run, the forces needed to hold the crack tip together are computed. For the second run, the nodes at the crack front are released and the displacement vector is determined. Both steps are necessary to calculate the strain energy release values and to decide either the crack is extended or not. The VCCT approach additionally assumes that crack growth does not significantly change the state at the crack tip, that is, the crack grows in a self-similar manner [28]. From this it follows, that the forces are still computed at the crack tip, but the displacement vector is taken at the neighbouring nodes of the crack front in the debonded area. Hence, only one computational run is necessary to compute the strain energy release rates. The strain energy release values at the crack front, seen on the left-hand side in Fig. 3, are computed according to (1-3).

Due to possible interactions of the different delamination modes (mode I, II and III), the extended B-K-criterion is applied to determine crack growth. This criterion is based on the original B-K (Benzeggagh-Kenane) mixed-mode failure criterion [4] which only combines mode I and mode II. This mixed-mode I/II interaction is demonstrated in Fig. 4. Due to a lack of mixed-mode data including mode III, Li [20] proposes to set the interlaminar fracture toughness values of G_{IIIc} equals to G_{IIc}. Both approaches, the original B-K law and Li's proposal for the interlaminar fracture toughness are combined

6
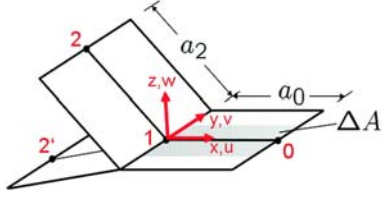
$$G_I = -\frac{1}{2 \cdot \Delta A} \cdot F_z(w_2 - w_{2'})\frac{a_0}{a_2} \qquad (1)$$

$$G_{II} = -\frac{1}{2 \cdot \Delta A} \cdot F_z(u_2 - u_{2'})\frac{a_0}{a_2} \qquad (2)$$

$$G_{III} = -\frac{1}{2 \cdot \Delta A} \cdot F_z(v_2 - v_{2'})\frac{a_0}{a_2} \qquad (3)$$

Figure 3: VCCT model with arbitrary rectangular shell elements and strain energy release rates
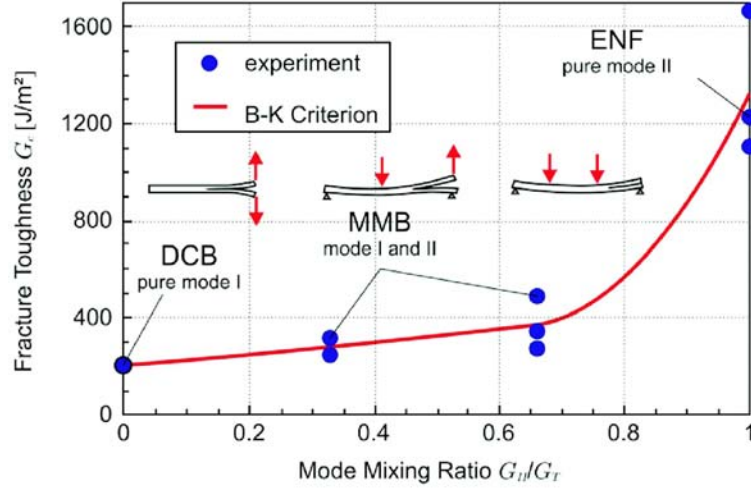
Figure 4: Original B-K-law [4] for mixed mode I-II. Graph taken from [18]

by Camanho and Dávila [6] to a three-dimensional criterion which is given in (4). When f reaches or exceeds 1 the existing crack in the interface is extended by releasing the respective MPCs.

$$f = \frac{G_I + G_{II} + G_{III}}{G_{Ic} + (G_{IIc} - G_{Ic})\left(\frac{G_{II}+G_{III}}{G_I+G_{II}+G_{III}}\right)^{\eta}} \qquad \begin{cases} < 1 & \text{no propagation} \\ \geq 1 & \text{propagation} \end{cases} \qquad (4)$$

The parameters used for interlaminar fracture toughness values and for the VCCT are set to $G_{Ic} = 0.243\,kJ/m^2$ and $G_{IIc} = G_{IIIc} = 0.514\,kJ/m^2$ and the curve fitting parameter $\eta = 1.81..$. The mixed-mode coefficient is taken from data in [15]. The ply damage degradation model is based on the extended Hashin [16] criteria as proposed by Goyal et al. [13]. These are used to predict occurrence of in-plane failure. The criteria of fibre failure, matrix

7

cracking and fibre-matrix shear failure are monitored and used to reduce a set of appropriate material properties, as proposed by Chang and Lessard [8], to ten per cent of the initial stiffness values. Since the energy release rate is up to the element size, the FE method may result in a mesh-dependency if regularisation procedures are not used [22, 23]. However, this is not taken into account in the present work. The criteria and the set of reduced properties for the different failure modes are summarised in Table 2.

4   Analyses of the nominal configurations

The global model as seen in Fig. 5 is generated with four-node shell elements. These are four-node, thick shell elements with global displacements and rotations as degrees of freedom. Bilinear interpolation is used for the coordinates, displacements and the rotations. The membrane strains are obtained from the displacement field and the curvatures from the rotation field. The transverse shear strains are calculated at the middle of the edges and interpolated to the integration points. In this way, it is a very efficient and simple element which exhibits correct behaviour in the limiting case of thin shells. Plane stress consideration omits the stress in through-thickness direction, namely σ_3, but strain in this direction, ε_3, is possible due to transverse contraction.

The modelled FE mesh contains three elements in both the stiffener's blade and each flange. In the region between two stiffeners the number of elements is set to 8. In longitudinal direction, 61 elements are used to obtain almost squared elements. The longitudinal displacements at the bottom end of the panel are fixed and at the opposite side displacement controlled compressive loading in longitudinal direction. The so-called potting constrains the displacements in the radial and circumferential direction and ensures even application of the compressive load. Both free edges are supported by constraining the circumferential displacement and rotation around the longitudinal axis. For investigations on postbuckling behaviour the obtained buckling shape by simulation has to match with the experimental buckling pattern. The buckling shape is highly sensitive to the applied boundary conditions, hence, it is important to represent the experimental boundary conditions in the FE model.

Table 2: Ply damage degradation model based on the extended Hashin [16] criteria as proposed by Goyal et al. [13]. Ply degradation model as proposed by Chang and Lessard [8]

Failure type		Criterion	Property reduced
Fibre fracture	$\sigma_1 \geq 0$	$f_F^2 = \frac{\sigma_1^2}{X_t^2}$	E_1, E_2, G_{12}, G_{23}, G_{13}
	$\sigma_1 < 0$	$f_F^2 = \frac{\sigma_1^2}{X_c^2}$	
Matrix cracking	$\sigma_2 \geq 0$	$f_M = \left(\left(\frac{\sigma_2}{Y_t} \right)^2 + \left(\frac{\tau_{12}}{S_{12}} \right)^2 \right)^{\frac{1}{2}}$	E_2
	$\sigma_2 < 0$	$f_M = \left(\frac{\sigma_2}{Y_c} \left[\left(\frac{Y_c}{2S_{23}} \right)^2 - 1 \right] \right.$ $\left. + \left(\frac{\sigma_2}{2\,S_{23}} \right)^2 + \left(\frac{\tau_{12}}{S_{12}} \right)^2 \right)^{\frac{1}{2}}$	
Fibre-matrix shear failure	$\sigma_1 \geq 0$	$f_{FM} = \left(\left(\frac{\tau_{12}}{S_{12}} \right)^2 \right)^{\frac{1}{2}}$	G_{12}, G_{23}
	$\sigma_1 < 0$	$f_{FM} = \left(\left(\frac{\sigma_1}{X_c} \right)^2 + \left(\frac{\tau_{12}}{S_{12}} \right)^2 \right)^{\frac{1}{2}}$	
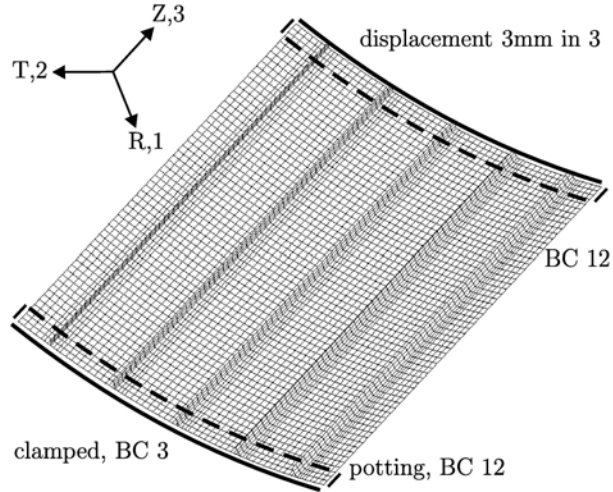
Figure 5: Generated four-node, thick shell element mesh and boundary condition (BC)

4.1 Intact configuration

Fig. 6 shows the out-of-plane displacements of the experimental test and contour plots of the simulation at different shortening levels. The picture of the experiment and the left contour plots are taken at a shortening level of 0.72 mm to compare the buckling shape. The intact panel shows the onset of skin buckling at 0.64 mm shortening, and by 1.00 mm a full pattern of skin buckles has developed, consisting of four to six buckling half waves per stiffener bay. The FE analysis predicts structural collapse of the entire panel due to catastrophic fibre fracture in two stiffeners very close to the lower potting at a shortening level of 2.47 mm. This failure is demonstrated in Fig. 8. The left picture shows the experiment after structural collapse. On the right-hand side, the picture depicts the outcome of the FE analysis. Good agreement is found in prediction of the failed part of the panel, where fibre fracture breaks the stiffeners.

The structural zooming analysis approach is an element refinement to achieve a better evaluation of the local behaviour of the global structure. Furthermore, it is time efficient due to little computational time of the local models which can be moved around to investigate several locations. In this case, the analysis is performed to detect locations where high through-thickness stresses occur which most likely lead to delamination initiation. Fig. 7 de-

10

picts a section of the generated local slice. The model represents a 4 mm
wide slice of the global panel. This slice is as wide as the stiffener's pitch
with half stiffener pitch length on each side of the blade. Every ply of the
laminate is modelled with 3-dimensional 8-node brick elements. The mesh in
the curved area underneath the stiffener's blade is automatically generated
with 3-D arbitrarily distorted brick elements. This finite element is an eight-
node, isoparametric, arbitrary hexahedral element. Trilinear interpolation
functions are used, where the strains tend to be constant across the element.
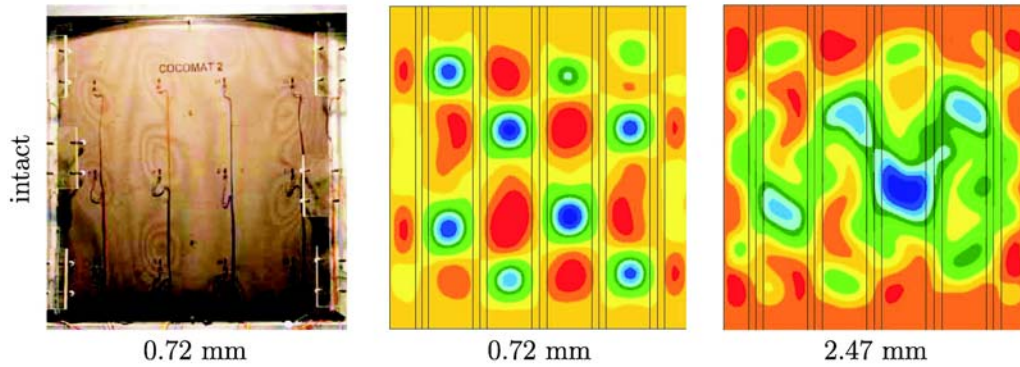
Figure 6: Out-of-plane displacements at applied shortening. Left: Intact
panel. Middle and Right: FE-Results.
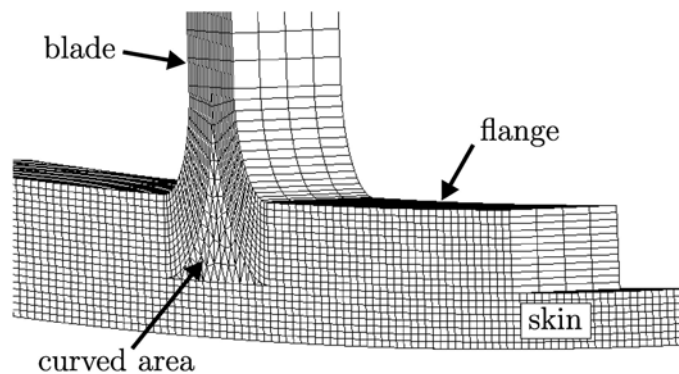
Figure 7: Section of the generated model for the structural zooming analysis

In Fig. 9 two different states of shortening levels are depicted. The black-
coloured bars demonstrate examples of locations where the local model is
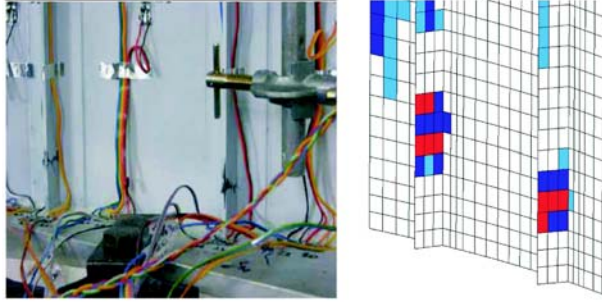
Figure 8: Ply failure in stiffeners close to the clamping. Experiment and FE analysis

moved to and high stresses are found. A total number of 11 locations have been investigated and classified. These 11 locations are distributed all over the entire panel, but only the three most critical locations, namely A, B and C and are depicted in Fig. 9. Both contour plots illustrate the mentioned locations where the buckling bends the skin away from the stiffener. However, location B is found as most critical during the compressive loading history.
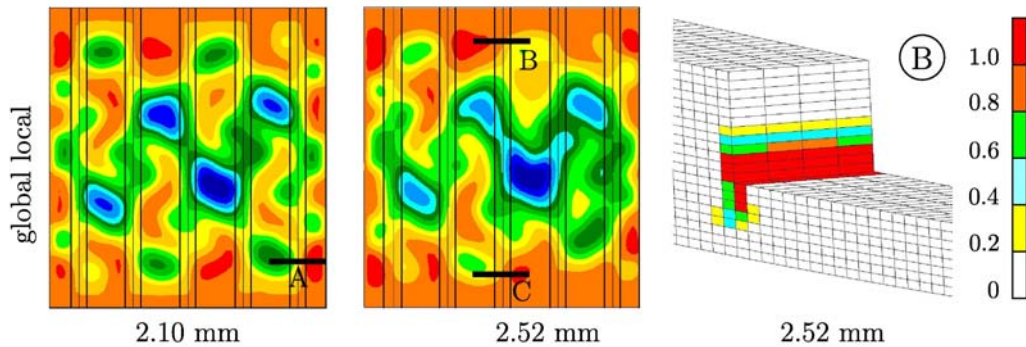
Figure 9: Structural zooming analysis: Locations to be found critical (black-coloured bars) demonstrated the local model

4.2 Pre-damaged configuration - version 1

The pre-damaged configuration of the multi-stiffener panel was proposed by the project partner IAI (Israel Aircraft Industries Ltd) and is denoted by *version 1* (V1). Three different types of pre-damaged areas are applied in

the skin-stiffener interface to investigate different effects. Fig. 10 illustrates contour plots of the panel at two different states of shortening where the black areas are the current state of debonding. The left contour plot shows the buckling shape at an early state and the black areas the initial debond length. The second plot shows the buckling shape close to structural collapse. The black-coloured areas have not changed in length, hence, no propagation of the initial interlaminar damage is predicted.
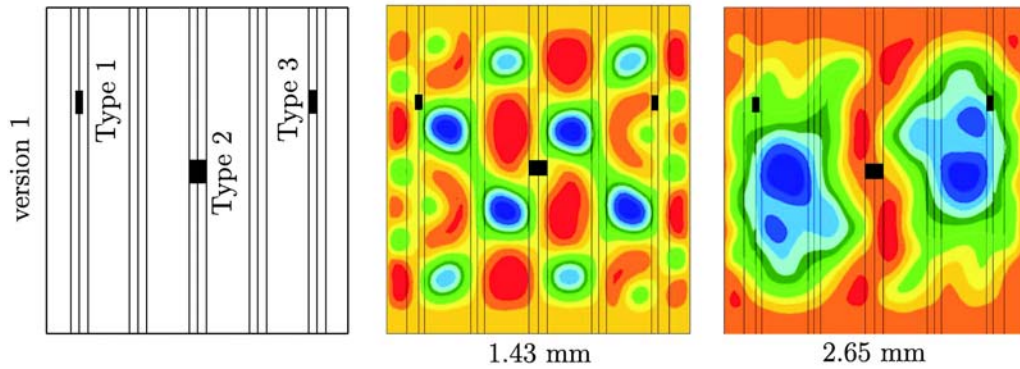
Figure 10: Pre-damaged configuration V1: Initial damage configuration and contour plots including the current state of debonding

4.3 Comparison with experiment

An intact and a pre-damaged configuration of the panel was manufactured by IAI and tested at the Technion, Israel. The panels were inspected ultrasonically following manufacture to ensure an appropriate panel quality. In the experimental tests, data acquisition was performed using displacement transducers (LVDTs), strain gauges and moiré fringes. The load-displacement curves of the intact configuration, experiment and FE simulation, are depicted in Fig. 11. The dotted line is the original curve obtained from the experiment. Due to imperfections in test conditions, e.g. delay between the loading machine and the panel, nonlinear behaviour can be observed at the beginning. Therefore, the original curve is shifted by 0.15 mm to find linear behaviour straight from the origin, illustrated by the dashed line. In comparison with the FE analysis (continuous line) a stiffer behaviour is observed up to the first buckling point. However, it is well-known that the FE method is capable of the stiffness prior to non-linearity. A very similar panel was

experimentally and numerically investigated using the same analysing tool as applied in this work and the results show very good agreement [26]. That evidences that the applied numerical tool can capture the initial stiffness, as well as the postbuckling behaviour. From this it follows, that the difference of the initial stiffness is obviously caused by the sensitivity of a structure to the applied boundary conditions, here in the potting area and at the longitudinal edge supports. U-shaped bars as longitudinal edge supports were applied in the test rig to represent the behaviour of an entire cylinder. These bars offer a little room of movement between them and the panel which has to be taken into account for the correct stiffness. There are several examples of elastic foundations set as boundary conditions to enable e.g. gliding in the potting areas. Hence, the initial stiffness can be influenced by the stiffness of the springs [21, 33, 31]. However, in this work springs are not used to adapt the initial stiffness, since the focus is on the effect of different predamages and their behaviour in the postbuckling region. In terms of investigating crack propagation, the buckling pattern is seen as most relevant and good comparison is found. At a load level of 88.2 kN the panel started to buckle during testings. The FE analysis predicts the first buckling point under a compressive load of 82.1 kN. From this it follows, that the numerical simulation leads to a discrepancy of seven per cent. Beyond the first buckling point good agreement is found to the experimental results until fibre fracture occurs. During the experiment at a shortening level of approximately 2.2 mm the panel popped out of the longitudinal edge support which affected the buckling pattern. However, the two locations where increased fibre fracture leads to the structural collapse is predicted very close to the locations where the blades failed during the experiment, see Fig. 8.

In the experiment the pre-damaged panel was not directly loaded up to collapse, but was cyclically loaded into the postbuckling region. The panel was loaded with 50,000 cycles up to 147 kN, then 10,000 cycles up to 177 kN with no damage observed. Nondestructive testing methods were used to assess the state of the skin-stiffener debonds, and no observable crack growth was detected. The cyclic load was then set to 196 kN, and at cycle 1,210 fibre fracture was seen in a stiffener near the potting. This was repaired using a local steel reinforcement, and the cycling at 196 kN was continued for another 6,000 cycles. At this point damage in the area around the skin was seen near the repaired location. The panel was then statically loaded to collapse, which occurred at 155 kN due to fibre fracture throughout the skin and stiffeners. The results in Fig. 12 show the load-displacement curve for cycle 61,500
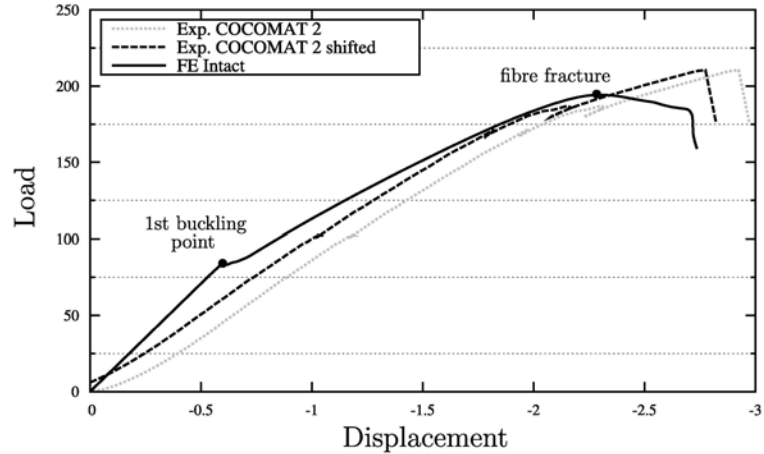
Figure 11: Load-displacement curves of the intact configuration: Experiment and FE analysis

where first fibre fracture occurred and the repair was required. Comparing the experiment with the simulation shows good agreement for both load-shortening curves and the absence of interlaminar damage propagation. The tested panel as well as the FE analysis shows no observable crack growth until structural collapse occurs. Independent of the debond width no pre-damage type led to crack growth. Thus, the key result from the experimental testing is that despite containing three skin-stiffener debonds, crack growth is not observed at these locations at any stage of the testing.

5   Damage Sensitivity

As the aim of the experimental testing was to obtain delamination growth, three alternative configurations were proposed. The sensitivity of the structure to different initial debonds, including type, location and length, is investigated to classify their criticality to interlaminar damage growth. The designated pre-damaged version 1 (V1) is taken as reference configuration for all performed modifications. Three further versions were proposed, namely versions 2 - 4 (V2 - V4) as shown in Fig. 13. V2 is based on V1 with a length of all debonds increased from 25 mm to 50 mm; V3, which is based on V2 but uses only full-width debonds and V4 is based on V2 but has all debonds located at the panel centreline. Fig. 13 shows the initial pre-damages and

15
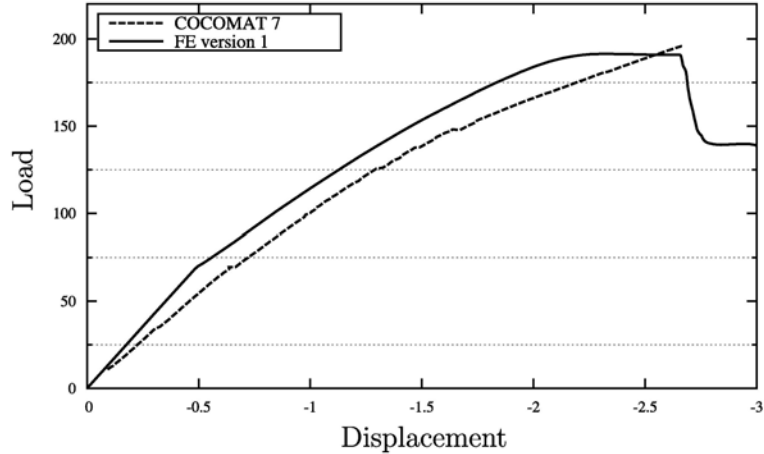
Figure 12: Load-displacement curves of the pre-damaged configuration version 1: Experiment and FE analysis

contour plots of two different states of loading. The black-coloured areas depict the current debonded length of the damaged regions.

5.1 Versions 2-4

V2 includes all three different types of initial debonds. The pre-existing debond lengths are doubled, compared to reference V2, to an initial length of 50 mm, but the locations and types are maintained. At a shortening level of 1.43 mm crack growth is initiated at the middle stiffener debond. This type 2 pre-damage propagates up to 216 mm at 2.15 mm shortening. Both upper debonds show no observable extension of interlaminar damage. The simulation of this panel is terminated at a shortening level of 2.15 mm due to extremely small load step sizes to obtain convergence. In terms of predicting observable interlaminar damage propagation, this state is regarded as sufficient.

The second proposal is denoted by pre-damaged V3 and offers only one type of pre-damage. Pre-damage type 2 is applied to all three predetermined locations with a length of 50 mm. At a shortening level of 1.19 mm at two locations crack growth is initiated. In the upper left corner the pre-existing debond is extended to 168 mm at a shortening level of 1.97 mm. Under the same compressive load the debond in the middle skin-stiffener interface grows to 198 mm length. This FE analysis is terminated at a shortening

16

level of 1.97 mm just like V2 due to identical reasons. The analysis predicts interlaminar damage propagation at two different locations, but on the same pre-damage type.

V4 includes all three different types of initial debonds with a common length of 50 mm, but the locations are varied compared to V2. At a shortening level of 1.46 mm the interlaminar damage propagation is initiated at the middle stiffener and at the stiffener on the right-hand side. Both initiated debonds show observable crack growth at a shortening level of 1.89 mm where the simulation is terminated. Debond type 3 is extended to 75 mm and type 2 to 132 mm. Thus, crack growth is predicted at two different locations where two different types of pre-existing damages are applied.

5.2   Comparison of the local and global behaviour

Fig. 14 shows the contour plots of the intact panel configuration and all versions of the pre-damaged configuration. Due to the termination of the simulations a common shortening level of 1.89 mm is chosen for comparison. At this state, the local behaviour of the buckling pattern and the interlaminar damage propagation are discussed.

The pre-damaged V1 offers no observable crack growth until structural collapse occurs. Comparison of the postbuckling pattern of the intact, which includes no pre-existing damaged regions, and the pre-damaged version with 25 mm long debonds shows no significant changes. That means that a debond length of 25 mm can be classified as critical for this type of stiffened structure, hence, small debonds do not significantly alter the buckling shape.
Pre-damaged V2 is based on V1, but the debond length is modified from 25 mm to 50 mm. Simulation of this version leads to crack growth at the debond located at the middle stiffener. Thus, a larger debond length leads to interlaminar damage propagation and affects the buckling shape as well. The differences between V2 and V3 are in the type of initial pre-damages. In panel V2 only the type 2 pre-damage, a full-width debond, is applied. The corresponding analysis predicts crack growth at two locations. This result indicates that a minimum allowable crack length for this panel design is at least 25 mm, and that small debonds do not significantly alter the buckling shape.
In terms of investigating different location with identical pre-damage types, V4 is investigated. V2 has all pre-existing interlaminar damages in a stag-

gered pattern, unlike V4 where all debonds are located at the centreline.

Fig. 15 shows several contour plots of the different versions. All the panels are compared at the final state of compression when the analysis is terminated. Even though all versions show a different buckling shape and each pre-damaged panel offers different final crack lengths and locations, the load-displacement curves, plotted in Fig. 16, show no significant differences. All five FE curves have the same initial stiffness up to the first buckling point. However, beyond the first buckling point all analysed versions offered a different buckling pattern. As the buckling shape could affect the stiffness different load-displacement curves are expected. At a shortening level of approximately 1.5 mm the pre-damaged versions V2, V3 and V4 show the onset of crack propagation and at this state little differences in stiffness can be observed. The comparison of all analysed panels shows that up to the point where crack growth is initiated, independent of the buckling shape, no differences in stiffness are found. All pre-damaged panels are as stiff as the intact configuration prior to crack extension. However, the different crack growth behaviour of the configurations illustrates the effect of damage location, and the critical way in which this interacts with the buckling shape. This has significant implicitations for the design of composite stiffened structures in compression, and indicates that the location of damage relative to the buckling shape is a key consideration for damage tolerance.
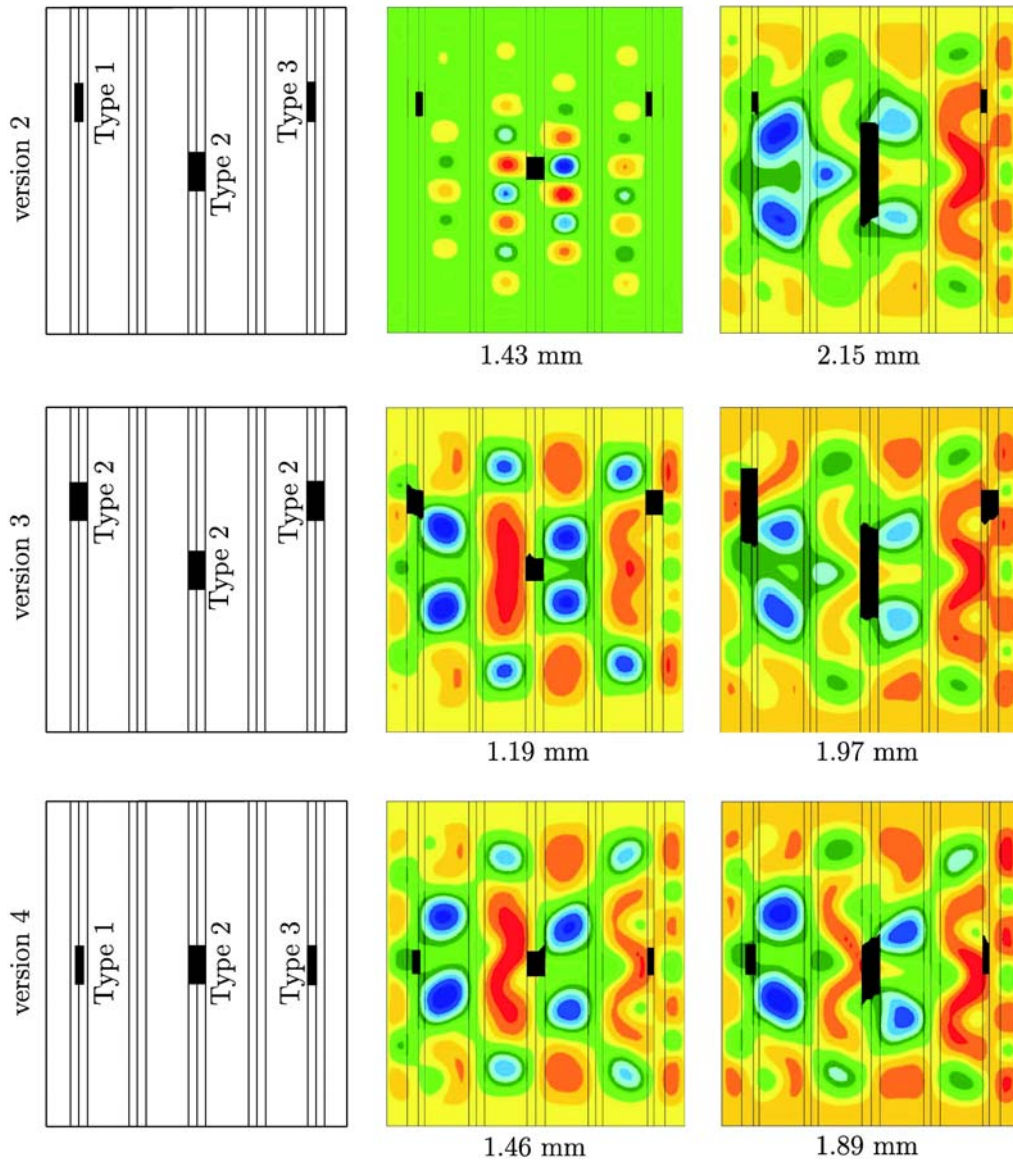
Figure 13: Pre-damaged V2 - 4: Initial damage configuration Contour plots including the current state of the debonded areas
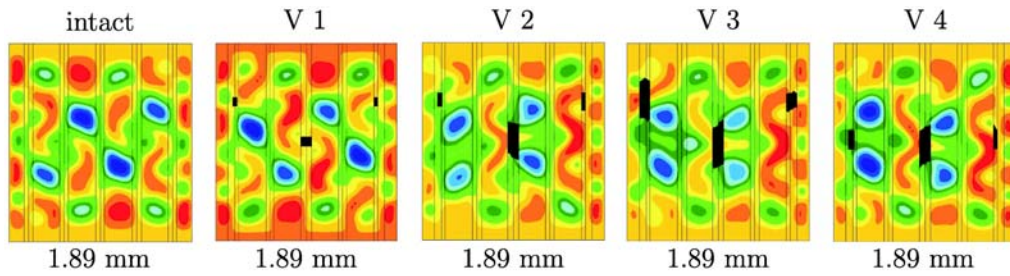
Figure 14: Comparison of the loacal behaviour at a shortening level of 1.89 mm: Intact and pre-damaged V1 - 4
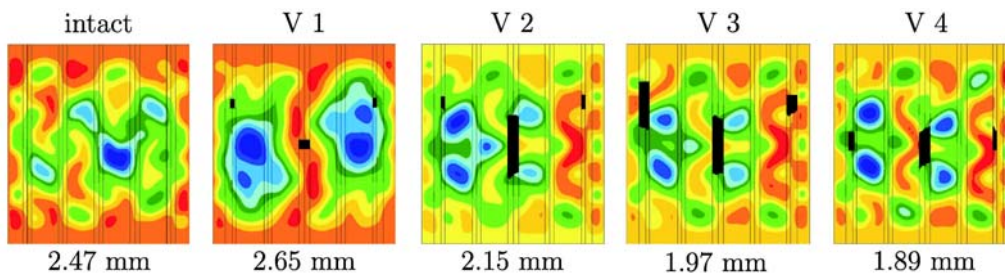
Figure 15: Comparison of the global behaviour at the final state: Intact and pre-damaged V1 - 4
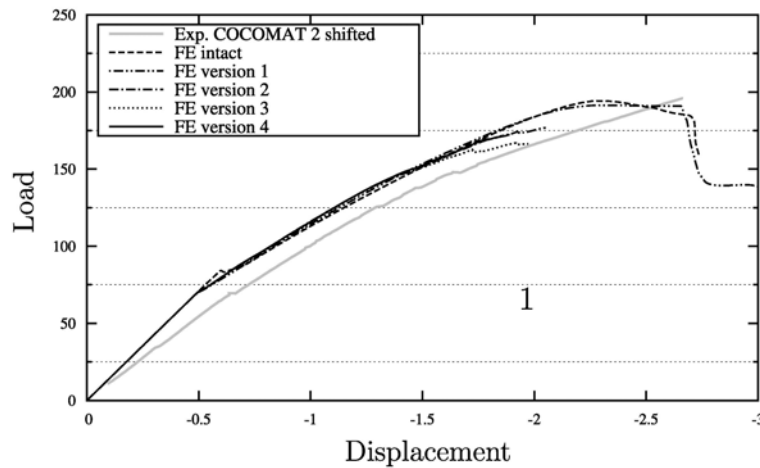
Figure 16: Comparison of the global behaviour at the final state: Intact and pre-damaged V1 - 4

6 Conclusions

The results indicate that the criticality of damage for a given panel design is not only dependent on the size of the damage, but also on its location. This has been proposed in the investigated panel configurations in terms of debonds of identical size, but in different locations. Such a modification yields much more critical crack growth. The criticality of a given debond is related to the crack opening displacements generated at the crack front, which are dictated by the deformation pattern of the panel. As such, the results are sensitive to the capability of the analysis to capture the correct displacements, which is especially relevant in postbuckling problems. The results suggest that damage size and location and the panel displacement pattern are critical factors for design and certification of postbuckling structures accounting for damage.

Acknowledgements

References

[1] *MSC.Marc - Vol A - Theory and User Information.*

[2] C. Balzani and W. Wagner. An interface element for the simulation of delamination in unidirectional fiber-reinforced composite laminates. *Engineering Fracture Mechanics of Composite Materials and Structures*, 75:2597–2615, 2008.

[3] G. I. Barenblatt. The mathematical theory of equilibrium cracks in brittle fracture. *Advances in Applied Mechanics*, 7:55–129, 1962.

[4] M.L. Benzeggagh and M. Kenane. Measurements of mixed-mode delamination fracture toughness of unidirectional glass/epoxy composites with mixed-mode bending apparatus. *Composite Science and Technology*, 56:439–449, 1996.

[5] R. Borg, L. Nilsson, and K. Simonsson. Modeling of delamination using a discretized cohesive zone and damage formulation. *Composites Science and Technology*, 62:1299–1214, 2002.

[6] P. P. Camanho, C. G. Dávila, and M. F. de Moura. Numerical simulation of mixed-mode progressive delamination in composite materials. *Journal of Composite Materials*, 37-16:1415–1424, 2003.

[7] P. P. Camanho, C. G. Dávila, and S. T. Pinho. Fracture analysis of composite co-cured structural joints using decohesion elements. *Fatigue & Fracture of Engineering Materials & Structures*, 27:745–757, 2004.

[8] F. K. Chang and L. B. Lessard. Damage tolerance of laminated composites containing an open hole and subjected to compressive loadings. *Journal of Composite Materials*, 25:2–43, 1991.

[9] R. Degenhardt, A. Kling, H. Klein, W. Hillger, H.C. Goetting, R. Zimmermann, and K. Rohwer. Experiments on buckling and postbuckling of thin-walled CFRP structures using advanced measurement systems. *International Journal of Structural Stability and Dynamics*, 7:337–358, 2007.

[10] R. Degenhardt, R. Rolfes, R. Zimmermann, and K. Rohwer. COCOMAT - improved material exploitation of composite airframe structures by accurate simulation of postbuckling and collapse. *Composite Structures*, 73:175–178, 2006.

[11] D. S. Dugdale. Yielding of steel sheets containing slits. *Journal of the Mechanics and Physics of Solids*, 8:100–104, 1960.

[12] S. Feih. *Design of composite adhesive joints*. PhD thesis, Cambridge University, 2002.

[13] V. K. Goyal, R. J. Navin, E. R. Johnson, and R. A. Damodar. Intralaminar and interlaminar progressive failure analyses of composite panels with circular cutouts. *Composite Structures*, 64:91–105, 2004.

[14] A. A. Griffith. The phenomenon of rupture and flow in solids. *Philosophical transactions of the Royal Society of London*, 221A:163–198, 1920.

[15] P. Hansen and R. Martin. DCB, 4ENF and MMB delamination characterisation of S2/8552 and IM7/8552. Technical Report N68171-98-M-5177, Materials Engineering Research Laboratory Ltd. (MERL), Hertford, UK, 1999.

[16] Z. Hashin. Failure criteria for unidirectional fiber composites. *Journal of Applied Mechanics*, 47:329–334, 1980.

[17] G. R. Irwin. *Handbuch der Physik*. 1958.

[18] R. Krueger. Virtual crack closure technique: History, approach, and applications. *Journal of Applied Mechanics*, 57:109–143, 2004.

[19] P. Ladevèze. A damage computational approach for composites: basic aspects and micromechanical relations. *Computational Mechanics*, 17:142–150, 1995.

[20] J. Li. Three-dimensional effect in the prediction of flange delamination in composite skin-stringer pull-off specimens. *Journal of Composites Technology & Research. JCTRER*, 24-3:182–189, 2002.

[21] P. Linde, A. Schulz, and W. Rust. Influence of modelling and solution methods on the FE-simulation of the post-buckling behaviour of stiffened aircraft fuselage panels. *Composite Structures*, 73:229–236, 2006.

[22] P. Maimí, P.P. Camanho, J.A. Mayugo, and C.G. Dávila. A continuum damage model for composite laminates: Part I – constitutive model. *Mechanics of Materials*, 39:897–908, 2007.

[23] P. Maimí, P.P. Camanho, J.A. Mayugo, and C.G. Dávila. A continuum damage model for composite laminates: Part II – computational implementation and validation. *Mechanics of Materials*, 39:909–919, 2007.

[24] A. Needleman. An analysis of tensile decohesion along an interface. *Journal of Mechanics and Physics of Solids*, 38:289–324, 1990.

[25] T. K. O'Brien. Fracture mechanics of composite delamination. In *ASM handbook 21, Composites*, pages 241–245. ASM International, 2001.

[26] A. C. Orifici. *Degradation models for the Collapse Analysis of Composite Aerospace Structures.* PhD thesis, Royal Melbourne Institute of Technology, 2007.

[27] A. C. Orifici, R. S. Thomson, R. Degenhardt, C. Bisagni, and J. Bayandor. A finite element methodology for analysing degradation and collapse in postbuckling composite aerospace structures. in press. doi:10.1177/ 0021998309345294. *Journal of Composite Materials*, 2008.

[28] S. Rinderknecht and B. Kröplin. A finite element model for delamination in composite plates. *Mechanics of Composite Materials and Structures*, 2:19–47, 1995.

[29] E. F. Rybicki and M. F. Kanninen. A finite element calculation of stress intensity factors by a modified crack closure integral. *Engineering Fracture Mechanics*, 9:931–938, 1977.

[30] L. Tong. An assessment of failure criteria to predict the strength of adhesively bonded composite double lap joints. *Journal of Reinforced Plastics and Composites*, 16 / 8:698–713, 1997.

[31] W. Wagner. Numerical simulation of DLR-benchmark: Axially compressed stiffened CFRP panel. In *R. Degenhardt - GARTEUR Open, SM, AG 25 - Postbuckling and Collapse Analysis - Benchmark 3 Evaluation Report and Collected Contributions*, IB 131-2003/29. Deutsches Zentrum für Luft- und Raumfahrt e.V., Braunschweig, Oktober 2003.

[32] W. Wagner and C. Balzani. Simulation of delamination in stringer stiffened fiber-reinforced composite shells. *Computers and Structures*, 86:930–939, 2008.

[33] R. Zimmermann, H. Klein, and A. Kling. Buckling and postbuckling of stringer stiffened fibre composite curved panels - tests and computations. *Composite Structures*, 73:150–161, 2006.